Wave Modulation of the Extratropical Tropopause Inversion Layer

Robin Pilch Kedzierski[1], Katja Matthes[1,2], and Karl Bumke[1]

[1]Marine Meteorology Department, GEOMAR Helmholtz Centre for Ocean Research Kiel, Kiel, Germany.
[2]Faculty of Mathematics and Natural Sciences, Christian-Albrechts-Universität zu Kiel, Kiel, Germany.

Correspondence to: Robin Pilch Kedzierski (rpilch@geomar.de)

Abstract.

This study aims to quantify how much of the extratropical Tropopause Inversion Layer (TIL) comes from the modulation by planetary and synoptic-scale waves. By analyzing high-resolution observations, it also puts other TIL enhancing mechanisms into context.

5   Using gridded COSMIC GPS-RO temperature profiles from 2007-2013 we are able to extract the extratropical wave signal by a simplified wavenumber-frequency domain filtering method, and to quantify the resulting TIL enhancement. By subtracting the extratropical wave signal, we show how much of the TIL is associated with other processes, at mid and high latitudes, for both Hemispheres and all seasons.

10   The instantaneous modulation by planetary and synoptic-scale waves is almost entirely responsible for the TIL in mid-latitudes. This means that wave-mean flow interactions, inertia-gravity waves or the residual circulation are of minor importance in mid-latitudes.

At polar regions, the extratropical wave modulation is dominant for the TIL strength as well, but there is also a clear fingerprint from sudden stratospheric warmings (SSWs) and final warmings in 15   both hemispheres. Therefore, polar vortex breakups are partially responsible for the observed polar TIL strength in winter (if SSWs occur) and spring. Also, part of the polar summer TIL strength cannot be explained by extratropical wave modulation.

After many modelling studies that proposed different TIL enhancing mechanisms in the last decade, our study finally identifies which processes dominate the extratropical TIL strength and 20   their relative contribution, by analyzing observations only. It remains to be determined, however, which roles the different planetary and synoptic-scale wave types play within the total extratropical wave modulation of the TIL; and what causes the observed amplification of extratropical waves near the tropopause.

1 Introduction

25 The extratropical Tropopause Inversion Layer (TIL) is a strong temperature inversion at the extra-
tropical tropopause with a corresponding static stability maximum right above. It is a fine-scale
feature discovered via tropopause-based averaging (Birner et al., 2002; Birner, 2006), consisting of
a thin layer of about 1km depth. Satellite Global Positioning System radio occultation observations
(GPS-RO) show that the TIL is present at all latitudes (Grise et al., 2010).

30 The TIL is established as an important feature of the extratropical upper troposphere and lower
stratosphere (UTLS) (Gettelman et al., 2011), and it is of interest to the scientific community for
the following reasons: high static stability values theoretically affect the dispersion relations of at-
mospheric waves like Rossby or Inertia-Gravity waves since this parameter is part of different wave
theory approximations (see Birner (2006); Grise et al. (2010) and references therein). In an ideal-

35 ized model experiment, Sjoberg and Birner (2014) showed that the TIL acts as a partial barrier for
upward wave propagation. The study by Zhang et al. (2015) supports this hypothesis by showing in-
hibited upward propagation of Inertia-Gravity waves (IGW) due to the TIL, with data from a single
US radiosonde station. Also, the TIL is likely to inhibit the cross-tropopause exchange of chemical
compounds: high static stability suppresses vertical motion and is correlated with strong trace gas

40 gradients (Hegglin et al., 2009; Kunz et al., 2009; Schmidt et al., 2010). In the next paragraphs we
shortly review what is known so far about the observed variability of the extratropical TIL and the
mechanisms proposed for its formation/enhancement.

Climatological studies about the seasonal, zonal-mean state of the TIL show that it reaches max-
imum strength during polar summer while it displays a weaker relative maximum in winter mid-

45 latitudes (Birner, 2006; Randel et al., 2007; Randel and Wu, 2010; Grise et al., 2010). From a
synoptic-scale perspective, the TIL in mid-latitude winter has very pronounced zonal structures, and
the TIL within ridges (anticyclones) in mid-latitude winter has the same strength or even higher than
any TIL observed in polar summer (Pilch Kedzierski et al., 2015). The cyclone-anticyclone modula-
tion with weaker-stronger TIL is found at all extratropical latitudes and seasons (Randel et al., 2007;

50 Randel and Wu, 2010; Pilch Kedzierski et al., 2015).

Different mechanisms are responsible for the formation/maintenance of the extratropical TIL:

- Radiative cooling below the tropopause by water vapor due to its strong gradient across the
tropopause acts to enhance the TIL (Randel et al., 2007; Hegglin et al., 2009; Kunz et al., 2009;
Randel and Wu, 2010), and a high-resolution model study by Miyazaki et al. (2010b, a) showed that

55 radiative effects are dominant in polar summer, while dynamics enhance the TIL otherwise.

- The downwelling branch of the stratospheric residual circulation was proposed to cause dynami-
cal heating above the tropopause and TIL enhancement in a model experiment by Birner (2010). The
first evidence of this was found by Wargan and Coy (2016) at high latitudes following major sudden
stratospheric warmings (mSSW), mainly caused by the convergence of the vertical component of the

60 residual circulation ($\overline{w*}$). During a mSSW there is an acceleration of the residual circulation, and the

enhanced $\overline{w*}$ convergence is the reason of the downward-propagating positive temperature anomaly (Andrews et al., 1987), which in turn enhances the high-latitude TIL once the signal reaches the lowermost stratosphere in winter or spring.

- Baroclinic waves and their embedded cyclones-anticyclones can enhance the TIL by tropopause lifting and cooling, and also warming above the tropopause in anticyclones from vertical wind convergence (from model experiments by Wirth (2003, 2004); Wirth and Szabo (2007); Son and Polvani (2007)). These synoptic-scale dynamics partly explain the seasonality and latitude-dependence of the extratropical TIL strength. Also, the baroclinic life-cycle experiment by Erler and Wirth (2011) showed the importance of baroclinic wave breaking events in enhancing the TIL. However, so far there is only observational evidence of the role of synoptic-scale dynamics in the cyclone-anticyclone modulation of the (weaker-stronger) TIL (Randel et al., 2007; Randel and Wu, 2010; Pilch Kedzierski et al., 2015).

- And finally, small-scale inertia-gravity waves (IGW) also play a role in enhancing the TIL. Kunkel et al. (2014) showed transient TIL modulation and enhancement from the presence of IGW's in a baroclinic life-cycle experiment, and proposed that this could persistently enhance/maintain the TIL via wave-mean flow interaction. This was confirmed in the study by Zhang et al. (2015), who showed that the strong wind shear found within the TIL lead to IGW breaking, downward heat flux and tropopause cooling (from a single US high-resolution radiosonde station).

The goal of our study is two-fold: 1) quantify how much of the TIL strength in the extratropics comes from its modulation by planetary to synoptic-scale waves, and 2) by subtracting the wave signal, to identify other processes that enhance the TIL and thereby make an observational confirmation of their relative contribution. Only modelling studies have looked at these processes thus far (reanalysis in the case of mSSW in Wargan and Coy (2016)), or their observation is very sparse (one single US high-resolution radiosonde station in the IGW study by Zhang et al. (2015)). Therefore it is of interest to put the roles of the different TIL enhancing processes, as enumerated above, into context by using high amounts of high-resolution global GPS-RO observations from the COSMIC mission (Anthes et al., 2008), which is the primary source of high-resolution observations of the temperature structure near the tropopause. It has to be pointed out that our focus is oriented on knowing the total signal of the extratropical (planetary to synoptic-scale) waves, rather than separating every possible wave type at each given time, which is not possible in practice given the highly variable background wind regimes in the extratropics (see section 2 for more details).

We extract the extratropical wave signal by wavenumber-frequency domain filtering of gridded GPS-RO data. Our method is similar to that of Pilch Kedzierski et al. (2016), who quantified the role of the different equatorial wave types in modulating and enhancing the tropical TIL. Compared to the equatorial wave filtering, the method in this study is adapted and simplified to account for the distinct wave spectrum and the highly varying wind regimes that are found in the extratropics. We explain how this is done, justifying the filter settings, in section 2; and we provide a proof of

concept in section 3, showing that our method is successful in representing the extratropical waves
and their TIL modulation. In section 4 we quantify the average signal of the extratropical waves as
100   well as the remaining TIL with this signal removed, for all seasons in the mid- and high-latitudes of
the Northern and Southern Hemispheres. We summarize and discuss our main findings in section 5.

2   Data and Methods

2.1   Datasets

We analyze GPS-RO temperature profiles measured by the COSMIC satellite mission (Anthes et al.,
105   2008). The effective physical resolution of GPS-RO retrievals is normally ∼1km, improving to-
wards the order of 100m in regions where the stratification of the atmosphere changes, such as the
tropopause and the top of the boundary layer, where high vertical resolution is most needed (Kursin-
ski et al., 1997). The COSMIC dataset is provided (interpolated) on a regular vertical grid with
100m spacing, from the surface up to 40km altitude. The vertical resolution and height range of
110   the COSMIC GPS-RO temperature profiles are comparable to radiosonde data, but with the advan-
tages of global coverage, high sampling density of ∼2000 profiles/day, and weather-independence.
Also, the accuracy of GPS-RO profiles is even higher than that of radiosondes (Anthes et al., 2008;
WMO, 1996). With the temperature profiles, vertical profiles of static stability are calculated as the
Brunt-Väisälä frequency squared (N^2 [s^{-2}]):

115   $$N^2 = (g/\Theta) \cdot (\partial\Theta/\partial z)$$

where g is the gravitational acceleration and Θ the potential temperature. The tropopause height
(TP_z) was calculated using the WMO lapse-rate tropopause criterion (WMO, 1957). Profiles with
unphysical temperatures or N^2 values (temperature <-150°C, >150°C or N^2 >100×$10^{-4}s^{-2}$) or
those where the tropopause was not found were excluded (< 1%).

120   We also use daily-mean vertical profiles of zonal winds from the ERA-Interim reanalysis (Dee
et al., 2011), for the years 2007-2013. To extract the extratropical wave signal from the GPS-RO
dataset, we first grid the profiles (see subsection 2.2) and then apply wavenumber-frequency domain
filters which require data on a regular longitude-time spacing (see subsection 2.3).

2.2   Gridding of GPS-RO profiles

125   The COSMIC GPS-RO temperature profiles at certain latitude bands are gridded daily, between
2007-2013, on a regular longitude grid with a 10° separation. The latitude bands chosen for this
study are 40°N and 40°S to represent the mid-latitudes, and 80°N and 80°S for polar latitudes. These
latitude bands were selected because they show the seasonal cycle of the tropopause and TIL best for
mid and high latitudes. Throughout section 4, results for the latitudes 40° and 80° will be disclosed

130 for both Hemispheres. The same analyses were performed for the latitude bands in between, 50°-
60°-70°, which have an intermediate behavior in each case.

At each grid point, the profiles of that day within +-5° latitude and +-5° longitude are selected
to calculate a tropopause-based weighted average temperature profile and the corresponding N^2
vertical profile:

135 $$T_{grid}(\lambda, Z_{TP}, t) = \sum_i w_i T_i(\lambda, Z_{TP}, t) / \sum_i w_i$$

$$N^2_{grid}(\lambda, Z_{TP}, t) = \sum_i w_i N^2_i(\lambda, Z_{TP}, t) / \sum_i w_i$$

where λ is longitude, Z_{TP} is the height relative to the tropopause and t is time. The weight w_i is
an exponentially-folding function that depends on the distance of the GPS-RO profile from the grid
center, taking longitude, latitude and time (distance from 12UTC):

140 $w_i = exp(-[(D_x/5)^2 + (D_y/5)^2 + (D_t/12)^2])$, where D are the distances in °longitude (x sub-
script), °latitude (y) and hours (t). The maximum distance allowed from the grid point in each di-
mension is: 5° longitude, 5° latitude, and 12 hours from 12UTC, respectively.

The gridded tropopause height (λ,t) is calculated with the same weighting of all profiles' tropopauses.
The gridded temperature and N^2 profiles are shifted, as the last step, from the tropopause-based
145 vertical scale onto a ground-based vertical scale from 5km to 35km altitude, obtaining a longitude-
height array for each day of 2007-2013.

Most often 2-3 profiles are selected for averaging at a grid point with these settings, although one
GPS-RO profile is sufficient to estimate a grid point. However, in 14.8% of the cases the algorithm
does not find any profile. To fill in the gaps, the longitude range to select the profiles is incremented
150 to +-10° instead of +-5°, and the latitude range is also incremented to +-7.5° instead of +-5°, which
then leaves a 1.8% of empty grid-points. For this minority, profiles are selected within +-1day and +-
15° longitude (and same latitude settings). In all cases the weighting function remains the same. The
remaining data gaps (0.06%) are filled by averaging neighbouring grid points (+-1 longitude grids,
then +-1 day grids). These exceptions are for a very small portion of the gridded data, and therefore
155 do not affect the retrieved wave signatures after filtering (the percentages showed in this paragraph
are for the Northern Hemisphere, and they are similar in the SH).

This gridding method is very similar to the one used by Pilch Kedzierski et al. (2016) in the
equator, developed after Randel and Wu (2005). The higher GPS-RO density in the extratropics
allowed for a narrower latitude range to select profiles around a latitude band in order to minimize
160 meridional smoothing of the extratropical TIL properties. The lower bottom of the vertical scale is
set to 5km to account for the lower extratropical tropopause heights compared to the equator.

Once gridded, for each latitude band, we end up with a daily longitude-time array of temperature
and N^2 for each level between 5-35km with 100m vertical spacing. With a daily temporal resolution,

this dataset resolves waves with periods of 2 days or longer, or frequencies of 0.5 cycles per day (cpd)
165   or lower, which is enough to capture all the planetary and synoptic-scale extratropical waves. Note
that the inertial frequency in the extratropics ranges from ∼1.3cpd at 40° latitude to 2cpd at the poles,
so inertia-gravity waves (IGW), with frequencies between the inertial and the much higher buoyancy
frequency, cannot be resolved with these settings (Andrews et al., 1987). However, by extracting the
combined planetary and synoptic-scale wave signal and substracting it later, we can indirectly infer
170   how important is the role of IGWs or other processes in enhancing the extratropical TIL.

2.3   Wavenumber-Frequency Domain Filtering

With the longitude-height-time array of gridded temperature and N^2 profiles obtained in the previous subsection 2.2, we make use of the freely available 'kf-filter' NCL function (Schreck, 2009) to
filter in the wavenumber-frequency domain. For each vertical level (from 5km to 35km height with
175   100m vertical spacing), we retrieve a longitude-time array which is detrended, tapered in time and
space-time bandpass filtered with a two-dimensional Fast Fourier Transform. This methodology is
analogous to that of Pilch Kedzierski et al. (2016), who filtered gridded equatorial GPS-RO data in
certain regions of the wavenumber-frequency domain, following the dispersion curves of the different equatorial wave types which have clear spectral signatures in those wavenumber-frequency
180   domains (Wheeler and Kiladis, 1999). In the remaining of this section we will explain how the filter bounds in the wavenumber-frequency domain were chosen in this study to adapt the method of
Pilch Kedzierski et al. (2016) to the extratropics.

The extratropical wave modes differ greatly from those at the equator: they are not equatorially
trapped and can propagate in any direction, the Coriolis parameter has to be taken into account,
185   and the zonal wind regimes in the extratropics are much more variable than the equatorial ones. At
sub-seasonal time-scales, the Northern Annular Mode (NAM) can alter the strength of the prevailing
westerlies in the extratropical troposphere and lowermost stratosphere; there is a strong seasonal
cycle in the stratosphere with very strong westerlies (several tens of m/s) within the winter polar
vortex, changing to easterlies (-10 to -20 m/s) in summer; and the polar vortex is disrupted very
190   quickly during major sudden stratospheric warmings (mSSW). These modes of variability of the
zonal winds in the extratropics have higher amplitude and frequency than any wind regime shifts
found at the equator, which has a relatively weak seasonal cycle, and the quasi-biennial oscillation
(QBO) in the stratosphere still has less amplitude and frequency compared to the polar winter vortex
- summer anticyclone. Background winds affect the propagation of waves, by doppler-shifting their
195   dispersion relations or even precluding their propagation, therefore it is of special importance to take
them into account in the extratropics.

We make a comparison of the dispersion curves of the extratropical Rossby wave under different
background zonal wind regimes in Figure 1. The Rossby wave dispersion relation is defined as the
most common form of large-scale wave disturbance found in the extratropics: a planetary wave

forced from the troposphere, and propagating vertically and zonally in a quasi-geostrophic flow. Assuming N^2 and background mean zonal winds ($\bar{U}$) to be constant, and no meridional propagation for simplicity, the following dispersion relation can be obtained (following Andrews et al. (1987)):

$$w = s\bar{U} - s\beta[s^2 + f^2/gh]^{-1}$$

where w is the frequency, s is the zonal wavenumber, f the Coriolis parameter, β its meridional derivative at a certain latitude (the Beta-plane approximation), g the gravity acceleration and h the equivalent depth. Since we assume no meridional propagation for simplicity, the meridional wavenumber is set to zero so it is absent in this formula (compared to Andrews et al. (1987)). The term ($s\bar{U}$) accounts for the doppler-shifting of the dispersion relation by the background zonal winds; and the (f^2/gh) term is an approximation to account for the vertical propagation of the wave.

In Figure 1, we show how the dispersion curve of a Rossby wave changes depending on its equivalent depth (different line types), and the background zonal mean winds (zero winds black, blue for easterlies, red for westerlies, see specific arrows outside the diagram). Note that each dispersion curve is not valid for the entire year for the Rossby wave. For example, a Rossby wave in winter would propagate following the red (10m/s) dispersion relation in the lowermost stratosphere (i.e. the bottom of the polar vortex); at higher levels (the core of the polar vortex) stronger westerlies are found and the same Rossby wave would propagate following the red (40m/s) curve. At some point in spring and autumn, the black curve ($\bar{U} = 0$ m/s) is theoretically valid, and so is the blue curve (-10m/s) in summer, with easterlies throughout the stratosphere.

The dispersion relations in Fig. 1 show the difficulty of defining a wave type in the extratropics: the dispersion curve for a given wave type (idealized Rossby wave in this case) can be in basically every possible place within the wavenumber-frequency domain, depending on the background winds. Therefore, it is impossible to define one filter to extract Rossby waves that is valid for the entire time period (2007-2013) and that could be used at all levels between 5 and 35km altitude.

We overcome this difficulty by simplifying the method of Pilch Kedzierski et al. (2016). Instead of defining certain dispersion curves, we use wide boxes in the wavenumber-frequency domain, only differentiating eastward-westward propagating oscillations with respect to the ground and their periods (faster 2-4 day waves; slower 4-25 day waves; and 30-96 day or quasi-stationary waves), which are displayed as the six grey boxes in Fig. 1. We also define a seventh filter for wavenumber zero (s = 0, brown box in the middle of the diagram in Fig. 1) for completeness. This way, the Rossby waves will be captured by one or another filter, independently of the background zonal winds.

With this method we prioritize knowing the total effect of planetary and synoptic-scale extratropical waves on the TIL, at the cost of not differentiating baroclinic, barotropic, standing, travelling (etcetera) wave modes. We find this to be a fair compromise, since our study targets TIL modulation and enhancement by extratropical waves (successfully, see sections 3, 4 and 5), and not to disclose particular properties of these waves.

If waves are present, their filtered signal is outstanding compared to the (unavoidable to filter) background noise, which appears as a continuum of low-amplitude fluctuations (Wheeler and Kiladis, 1999), and the instantaneous modulation of the tropopause and the TIL by these waves will be captured since these oscillations are resolved by the gridded dataset (see subsection 2.2).

240 As mentioned above, the extratropical wave anomalies are filtered from a longitude-time array: each vertical level of the gridded GPS-RO profiles is filtered independently, and then stored together in a longitude-height-time array of wave anomalies. Therefore, for a given latitude band, we end up with arrays of gridded GPS-RO profiles (temperature and N^2), and the corresponding anomalies (also of temperature and N^2) from the seven wave filter bounds defined in Fig. 1, all gridded with

245 10° longitude, 100m height and 1-day spacing.

When one specific day is selected from these arrays, a longitude-height snapshot of the wave anomalies is obtained. Extratropical waves have vertical tilts in their temperature structures, and if the anomalies are large, they can effectively modulate tropopause height as explained next.

Figure 2 shows idealized temperature anomalies associated to an atmospheric wave with west-

250 ward vertical tilt, as a longitude-height snapshot of the positive/negative (red/blue dashed contours) temperature anomaly structures. The anomalies sketched in Fig. 2 would correspond to that of an upward-propagating Rossby wave (Andrews et al., 1987) which is present around the extratropical tropopause. Any tropospheric or stratospheric anomalies are omitted for simplicity in Fig. 2, since they are irrelevant for the instantaneous modulation of the TIL.

255 The tropopause is usually the coldest point in the uppermost troposphere, and the lapse-rate in the lower stratosphere is close to zero in the extratropics, therefore the wave temperature anomalies of high amplitude could shape the zonal tropopause height as depicted by the thick grey line in Fig. 2. The tropopause would fall above negative stratification anomalies, and/or below positive stratification anomalies, which in our idealized case is most often centered at the strongest negative

260 temperature anomalies (where present).

Note that the tropopause modulation by atmospheric waves sketched in Fig. 2 is highly idealized: usually waves with different wavenumbers, frequencies and vertical tilts can be present simultaneously, making the actual observed tropopause modulation more complex than in Fig. 2.

A tropopause-based mean of the anomalies sketched in Fig. 2 would yield a dipole of cold anoma-

265 lies centered at the tropopause, warm anomalies above, and a net TIL enhancement just from the presence of the wave in the tropopause region. Note that the ground-based zonal average temperature profile and the zonal mean tropopause height would remain the same despite the presence of wave anomalies in Fig. 2: only the tropopause-based zonal mean profile is affected.

We expect that our filtered wave anomalies will modulate the tropopause in a similar fashion as

270 sketched in Fig. 2 for temperature. Once a wave is away from the tropopause region or dissipated, no filtered signal will affect the TIL, therefore permanent effects from wave-mean flow interaction (wave dissipation or breaking) are not quantified by our method.

Next in section 3, we show examples of the filtered signals and the tropopause adjustment to the extratropical waves, in order to proof the validity of our method to study the extratropical TIL wave modulation.

3 Proof of Concept

Figure 3 shows snapshots of the longitude-height N^2 anomalies (colors) filtered in the wavenumber-frequency domains defined in Fig. 1 (see previous subsection 2.3), together with the tropopause height (black line), for the 50°N latitude band. Each snapshot is selected for a different winter date, in order to portray cases when there is a clear modulation of the tropopause's zonal structures from the extratropical wave anomalies. We do not include the s=0 filter since it lacks zonal structures by definition. In Fig. 3 the eastward and westward propagation refers to the movement of the wave relative to the ground as defined in subsection 2.3.

In Fig. 3 there are several analogies to the tropopause and TIL modulation by equatorial waves described in the study by Pilch Kedzierski et al. (2016). In our extratropical case, we also show tropopause modulation by the wave anomalies when their amplitude is large, with predominant positive N^2 anomalies above the tropopause, and negative N^2 anomalies below, which correspond to the temperature anomalies that modulate tropopause height as sketched in Fig. 2. The modulation by extratropical waves is especially clear in Fig. 3c for eastward-propagating waves with periods of 4-25 days: strong positive N^2 anomalies are detected right above the tropopause between -180°E and -25°E, while negative N^2 are located below the tropopause between 25°E and 180°E. Similarly, in Fig. 3d (westward-propagating 4-to-25-day waves) tropopause height follows the positive N^2 anomalies between -75°E and 180°E. Sometimes positive N^2 anomalies can be located below the tropopause and viceversa, as in the cases shown in Fig. 3 a, b, e and f; but the zonal mean is still dominated by positive N^2 anomalies right above the tropopause. Note that the different wave types in Fig. 3 can be present at the same time, so some tropopause zonal structures in the snapshots can be the result of modulation by another wave type.

It can also be observed in all cases in Fig. 3 that there is a relative maximum of wave activity around the tropopause regardless of the amount of wave activity in the stratosphere, as measured by N^2 anomalies. This is in line with the findings of Pilch Kedzierski et al. (2016) who reported wave amplification near the tropopause for every equatorial wave type.

The westward tilt of the Rossby waves can be discernible in many cases (Fig. 3 a-d) throughout the stratosphere: most clearly in the intermediate periods of 4-25 days which are the most common for travelling Rossby waves, but also visible sometimes in the 30-96 day periods, indicating the presence of quasi-stationary Rossby waves. This is a good indicator that these waves are properly captured by our filters, which are used at each vertical level independently: the vertical structure of the waves is obtained without filtering in the vertical direction. Note that in Fig. 3, planetary and

synoptic-scale waves are all superimposed, so the overall appearance is increasingly patchy when short and fast waves are present, which is why Fig. 3 e and f show these structures the most.

310 The wavenumber-frequency domain filtering method used for extratropical waves (see subsection 2.3 and Fig. 1), although simplified compared to Pilch Kedzierski et al. (2016) and unable to differentiate particular wave types, is able to capture the overall planetary and synoptic-scale extratropical wave signal and how it modulates the tropopause and the TIL as shown in Fig. 3.

The examples shown in Fig. 3 are for the 50°N latitude band in winter, but similar conclusions
315 can be drawn from any extratropical latitude or season. The tropopause-based, seasonal mean of the extratropical wave signal will show an overall TIL enhancement, which is quantified next in section 4 for mid and high latitudes, winter and summer, Northern and Southern Hemisphere.

4   Wave Modulation of the Extratropical Tropopause Inversion Layer

Figure 3 in section 3 showed the tropopause adjustment to the horizontal and vertical structure of
320 the filtered extratropical wave anomalies, with positive N^2 anomalies generally placed above the tropopause, and negative N^2 anomalies below. Therefore, a tropopause-based average of the wave signals should give a net TIL enhancement. We perform the same analysis with the filtered temperature anomalies, which we expect to show a net tropopause cooling and a warm anomaly aloft (the dipole needed to enhance N^2 right above the tropopause). When using the terms cooling/warming,
325 we refer to the net effect of extratropical waves on the tropopause-based zonal mean profile, since certain levels are cooler/warmer in the seasonal mean profile due to these waves.

Also, by substracting the extratropical wave signal from the gridded GPS-RO data, it is possible to show the remaining TIL that is caused by mechanisms other than the extratropical wave modulation. We will present the daily evolution of the vertical tropopause-based N^2 profile, comparing the
330 observed N^2 vertical structure to the one without the extratropical wave signal, which should show a weaker TIL.

Note that the wavenumber-frequency domain filters are not able to extract the wave anomalies at the beginning and end of the 2007-2013 time-period of our study. The highest period filtered is 96 days (see section 2, Fig. 1), therefore data from the first 100 days of 2007 and the last 100 days of
335 2013 are not used for any figures of this section, in order to make sure that there is no signal missing.

Throughout this section, we will present the two kinds of analysis explained in the previous paragraphs: seasonal, tropopause-based averages of the extratropical wave temperature and N^2 signals; and the time evolution of observed N^2 zonal-mean profiles, with and without the daily extratropical wave signal. Both analyses will be presented for mid-latitudes (40°N, subsection 4.1) and polar lati-
340 tudes (80°N, subsection 4.2), first in the Northern Hemisphere, and then the exact same methodology is applied to the same latitude bands in the Southern Hemisphere (80°S in subsection 4.3; 40°S in Appendix A).

4.1 Northern Hemisphere Mid-latitudes

Figure 4 shows the seasonally averaged signature of the different extratropical wave types (defined in
subsection 2.3, figure 1) at 40°N, as their mean anomaly in the tropopause-based zonal-mean vertical
profiles of temperature (left column) and N^2 (right column). All the defined extratropical wave types
show a cooling effect maximizing at the tropopause (Fig. 4 a and c), and a N^2 increase directly
above the tropopause (Fig. 4 b and d). This is also in line with the findings by Pilch Kedzierski et al.
(2016), who found the same effect of all equatorial wave types on the tropical TIL, only varying
in the amplitude of the mean wave signature. The mean wave signatures in Figure 4 show that
extratropical waves enhance the TIL in a very similar manner by tropopause adjustment to the wave
signal and the resulting cooling of the tropopause (and warming above to a lesser degree).

In Fig. 4 (a-d), the strongest signal belongs to eastward-propagating waves with periods of 4 to
25 days (red lines), in both winter (top row) and summer (bottom row). Baroclinic Rossby waves,
the most common wave type occuring at mid-latitudes (with prevailing westerlies during all year
at near-tropopause level, therefore their eastward propagation respect to the ground), fit within this
broadly defined wavenumber-frequency domain. This also explains why the extratropical wave sig-
nal is stronger in winter at mid-latitudes, since the mid-latitude jet strength and the baroclinic wave
activity both peak there during winter. We also note that quasi-stationary waves (periods of 30-96
days, black and dashed magenta lines) and the s=0 wave type (grey line) play a minor role in en-
hancing the TIL.

The total extratropical wave signal (Fig. 4 e and f) at 40°N is a tropopause cooling of ∼3.5K and
a TIL enhancement of ∼1.6×$10^{-4}s^{-2}$ in winter (red line). In summer (black line) the modulation
is weaker: tropopause cooling of ∼2.3K and ∼1.1×$10^{-4}s^{-2}$ of TIL enhancement. The total extra-
tropical wave signature in NH mid-latitude summer has a very similar magnitude compared to the
equatorial wave signal obtained by Pilch Kedzierski et al. (2016).

Figure 5a shows the daily evolution of the tropopause-based N^2 profile (2007-2013) at 40°N. In
Fig. 5a the TIL is clearly discernible in winter with higher N^2 values right above the tropopause,
ranging between 5.5×$10^{-4}s^{-2}$ (orange) and 6.5×$10^{-4}s^{-2}$ (red). Above the TIL in winter, the low-
ermost stratosphere has a relative minimum in N^2 of ∼3.5×$10^{-4}s^{-2}$ centered at 15km height,
and levels higher than 18km have N^2 values of ∼5×$10^{-4}s^{-2}$. In summer months the tropopause
is higher, and although the TIL and the stratospheric N^2 values are separated by a weak relative
N^2 minimum (white, blueish sometimes), both layers have N^2 values of 5-5.5 ×$10^{-4}s^{-2}$ (yellow,
orange sometimes). Fig. 5a agrees with previous climatologies of the mid-latitude N^2 vertical struc-
ture (e.g. Birner (2006); Grise et al. (2010)), while also showing its short-term variability without
time-averages.

Fig. 5b shows the same N^2 profile evolution, but with the daily extratropical wave signal sub-
tracted, therefore displaying the tropopause-based N^2 structures without the instantaneous modu-
lation by planetary to synoptic-scale extratropical waves. Therefore, any TIL observed in Fig. 5b

380 should be caused by other processes. It can be observed that the TIL in Fig. 5b is almost completely gone: N^2 right above the tropopause is always lower than the stratospheric values above 18km. However, in winter and spring a very weak relative maximum of N^2 can be observed above the tropopause (4-4.5 $\times 10^{-4} s^{-2}$, white and light-blue colors compared to the N^2 minimum of $3.5 \times 10^{-4} s^{-2}$ at 15km height), occasionally reaching N^2 values close to $5 \times 10^{-4} s^{-2}$ (sparse light-

385 yellow spots) in late winter and spring. In summer, there is no relative N^2 maximum above the tropopause at all in Fig. 5b.

The conclusion that Fig. 5b gives is that most of the mid-latitude TIL is explained by the instantaneous modulation by planetary to synoptic-scale extratropical waves. Other possible sources of TIL enhancement in the extratropics like IGW modulation, wave-mean flow interactions of any

390 wave type, residual circulation or radiative effects; all together they play a minor role in forming the zonal-mean TIL structure. The TIL enhancement by IGWs (Zhang et al., 2015) can be of importance locally in space and time, but its contribution to the zonal-mean TIL (even if it explained all the structures in Fig. 5b) would be less than the effect of the filtered planetary and synoptic-scale extratropical waves.

395 Separating the different extratropical wave types and their contribution to TIL enhancement is beyond the scope of this study, but of interest for future research. Two questions arise from our results:

1) Which wave type is dominant? Figs. 3 and 4 point towards the baroclinic Rossby wave, the most common and strongest wave type occurring in the extratropics, and we find the biggest signals

400 in the broad wavenumber-frequency domain that would include this wave type, but this still needs robust confirmation. Our current method would need significant refinement to separate the baroclinic Rossby wave from other wave modes present in the extratropics.

2) Which is the process that leads to the amplification of extratropical waves next to the tropopause level? This is visible in Fig. 3 for all wave types defined in subsection 2.3, and analogous to the near-

405 tropopause amplification of all equatorial wave types in the tropics observed by Pilch Kedzierski et al. (2016). It would be of high interest to know whether this amplification follows Linear Wave Theory (Andrews et al., 1987) or not.

The conclusions from this subsection for 40°N also apply to the Southern Hemisphere. The equivalent analyses for 40°S can be found in Appendix A.

410 **4.2 Northern Hemisphere Polar latitudes**

We proceed to apply the same analysis from the previous subsection 4.1 to polar latitudes. Figure 6 shows the seasonal average signature of the different extratropical wave types (defined in subsection 2.3, Fig. 1) at 80°N, as their mean anomaly in the tropopause-based zonal-mean vertical profiles of temperature (left column) and N^2 (right column). As in mid-latitudes (subsection 4.1), all the

415 defined extratropical wave types show a cooling effect maximized at the tropopause (Fig. 6 a and

c), and a N^2 increase right above the tropopause (Fig. 6 b and d). However, at polar latitudes the seasonality of the extratropical wave forcing is inverted compared to mid-latitudes. The total wave signatures in Fig. 6 e and f are weaker in winter (red line), with a tropopause cooling of $\sim$2.6K and a TIL enhancement of $\sim$1.1$\times$10$^{-4}s^{-2}$, similar to that found in mid-latitude summer. In summer (black line), there is a total tropopause cooling of $\sim$3.9K and a TIL enhancement of $\sim$1.9$\times$10$^{-4}s^{-2}$, similar to that found in mid-latitude winter.

Note that in Fig. 6 (a-d) the eastward-propagating 4-25 day band (red line) is no longer as dominant as in Fig. 4. This can be explained by the fact that zonal mean westerly winds are weaker at polar latitudes, therefore the wave spectrum does not get Doppler-shifted as much as at mid-latitudes, and more waves are observed to be westward-propagating with respect to the ground. As to why the extratropical wave signature is stronger in polar summer, as opposed to mid-latitudes (stronger in winter), we explain the inverted seasonalities by the position of the jet stream and the baroclinic wave activity, which migrate polewards in summer while being at the mid-latitudes in winter. However, it is still surprising that the total extratropical wave signature on the TIL region is of the same magnitude at mid-latitudes and polar latitudes, despite the opposed seasonal cycles as explained above. Since the meridional temperature gradients and the jet stream are weaker in summer, one would expect the extratropical wave signature on the TIL to follow this tendency. It is possible that extratropical waves at polar regions get amplified near the tropopause and reach the same amplitude as at mid-latitudes (at opposing seasons), but as noted in subsection 4.1 this amplifying mechanism near the tropopause needs further research.

Figure 7a shows the daily evolution of the tropopause-based N^2 profile (2007-2013) at 80°N. There is a distinct TIL throughout the year, with N^2 values right above the tropopause of $\sim$5$\times$10$^{-4}s^{-2}$ in winter (white to yellow colors) and between 7-8 $\times$10$^{-4}s^{-2}$ in summer (brown and black sometimes). Stratospheric N^2 values are around 4$\times$10$^{-4}s^{-2}$ (dark and light blue) at levels within 14-26km height, with increasing N^2 at higher levels. The N^2 structures showed in Fig. 7a (as in Fig. 5a) agree with previous climatologies of the high-latitudes N^2 vertical structure (Birner, 2006; Grise et al., 2010), and the daily temporal resolution shows the high variability associated with sudden stratospheric warmings (SSWs) in the stratosphere. Higher N^2 values in the stratosphere are observed during SSWs, with positive N^2 anomalies propagating downward and reaching the TIL region. The SSWs signals at particular events will be discussed next, since they will be easier to differentiate once the extratropical wave signal is removed in Fig. 7b.

Fig. 7b shows the N^2 profile evolution without the daily extratropical wave signal, displaying the tropopause-based N^2 structures caused by other processes. The TIL in Fig. 7b is significantly weakened without the extratropical wave modulation: in winter it almost disappears, but in summer the TIL is still distinct (5-6 $\times$10$^{-4}s^{-2}$, yellow and orange) from the background stratospheric N^2 structure (blue). The extratropical wave modulation explains an important part of the TIL's N^2 structure in polar latitudes (a similar amount of N^2 enhancement as in mid-latitudes, with inverted

seasonality, Fig. 6), but other sources of TIL enhancement are also present as it can be observed in Fig. 7b (unlike in Fig. 5b for mid-latitudes, where almost no TIL is visible without the extratropical wave signal). Most notably, the removal of the extratropical wave signal makes the time evolution of the vertical N^2 structures in Fig. 7b much smoother compared to Fig. 7a, and allows a clearer appearance of the downward-propagating signal from SSWs and how it affects the tropopause region. In Fig. 7b, major SSW events are marked with black arrows (2008, 2009, 2010, 2013), and one minor event is marked with a grey arrow in 2012. The major SSW event from February 2007 is not marked, since the first 100 days of 2007 are cut off for the analyses in this section.

During major SSWs, the residual circulation is accelerated, and the convergence of its vertical component ($\overline{w*}$) forces a positive temperature anomaly that propagates downward into the lowermost stratosphere (Andrews et al., 1987). In the study by Wargan and Coy (2016) it was shown that $\overline{w*}$ convergence is associated with a downward-propagating positive N^2 anomaly as well, that enhances the TIL once the SSW signal reaches the tropopause region. Wargan and Coy (2016) calculated a $\sim 1.5 \times 10^{-4} s^{-2}$ increase of the zonal-mean N^2 maximum above the tropopause due to the 2009 major SSW, and slightly lower N^2 increases in other SSW cases. In Fig. 7b, it can be observed that N^2 right above the tropopause in early 2009 increases from $\sim 4 \times 10^{-4} s^{-2}$ (blue) before the SSW, up to $\sim 5.5 \times 10^{-4} s^{-2}$ (orange) after the SSW. Also, a positive N^2 anomaly from the 2009 major SSW can be seen in Fig. 7b propagating downwards throughout the stratosphere (white and yellow instead of blue), and the TIL enhancement coincides with the time when this downward-propagating anomaly reaches the tropopause region, as well as a marked decrease in the zonal-mean tropopause height. This perfectly fits the findings of Wargan and Coy (2016). In Fig. 7b the same can be observed in the major SSW cases of 2008, 2010 and 2013, although the N^2 anomalies are slightly lower than in 2009 which was an exceptionally strong event.

Interestingly, in Fig. 7b we observe the downward-propagating positive N^2 anomaly, TIL enhancement and tropopause lowering in a minor SSW in early 2012, and also during the final warmings of 2011 and 2013. The coherency in time of these signals, and their similarity to the cases described by Wargan and Coy (2016) suggests that they are also driven by an acceleration of the residual circulation (increased $\overline{w*}$ convergence) from the disturbed polar vortex. The 2013 case is quite particular: once the major SSW is finished, the polar vortex recovers, the TIL is no longer enhanced and the tropopause slowly increases its height; but then there is a strong final warming event, another downward-propagating N^2 signal, immediate TIL enhancement and a slight lowering of the zonal-mean tropopause. After this, the zonal-mean tropopause gets steadily higher into the summer. In the final warming of 2011 there is an abrupt transition from a strong polar vortex to anticyclonic circulation, and the downward-propagating N^2 signal, TIL enhancement and abrupt zonal-mean tropopause lowering is also visible in Fig. 7b. In the case of the minor SSW of 2012, the TIL enhancement and zonal-mean tropopause lowering are also in clear coincidence with the disrupted westerlies.

490   Figure 7b shows evidence, directly from observations, that the TIL is enhanced due to major

SSWs, and also from other polar vortex disturbances: minor SSWs and abrupt final stratospheric

warmings. The similarity of our results with Wargan and Coy (2016), who studied major SSWs,

in terms of the time evolution of the N^2 signal, TIL enhancement and tropopause height; suggests

that accelerated residual circulation (increased $\overline{w*}$ convergence) is the main contributor to TIL en-

495   hancement during all kinds of polar vortex disturbances, not only major SSWs. This would need

confirmation with a more detailed study of (non-major) polar vortex disturbances and the associated

residual circulation variability.

Fig. 6f showed TIL enhancement of $\sim1.1\times10^{-4}s^{-2}$ by extratropical wave modulation in polar

winter. In Fig. 7b, we show that polar vortex disturbances in general can enhance the TIL in winter

500   (major and minor SSWs) and spring (final warmings) with a similar magnitude. The remaining

TIL in polar summer in Fig. 7b ($\sim5.5\times10^{-4}s^{-2}$, orange) is not explained by extratropical wave

modulation, nor by residual circulation. The only other mechanism restricted to polar summer that

could enhance the TIL is water vapor radiative cooling of the tropopause (Randel and Wu, 2010;

Miyazaki et al., 2010b), but this would also require an additional study to be confirmed.

505   We also note that the meridional advection of the SSW signals in the lowermost stratosphere

could be the cause of the very weak hints of the mid-latitude TIL without the extratropical wave

signal found in Fig. 4b, that mainly appears in late winter and spring and was strongest in 2009,

2010 and 2013, coinciding with major SSW events.

Given that the polar vortex behavior affects the TIL more clearly at polar latitudes, we expect more

510   differences between the NH and the SH, since the polar vortex in the SH is much less disturbed than

in the NH, and the only mSSW observed in the SH happened in 2002.

4.3 Southern Hemisphere Polar latitudes

Figure 8 is the Southern Hemisphere (SH) equivalent of Fig. 6. The total extratropical wave signal

at 80°S (Fig. 8 e and f) is a tropopause cooling of ~1.4K and a TIL enhancement of $\sim0.9\times10^{-4}s^{-2}$

515   in winter (compared to $\sim1.4\times10^{-4}s^{-2}$ TIL enhancement in the NH in Fig. 6). In summer there is

a tropopause cooling of ~2.5K and $\sim1.3\times10^{-4}s^{-2}$ of TIL enhancement ($\sim1.9\times10^{-4}s^{-2}$ in the

NH, Fig. 6). The extratropical wave signatures in Fig. 8 show the same seasonality as in Fig. 6, with

stronger (weaker) signals in summer (winter) months, but the overall magnitude of the extratropical

wave forcing at polar latitudes is lower in the SH than in the NH.

520   The lower extratropical wave activity and the smaller mean signal at the tropopause near the

South pole is explained by the isolation of the SH polar latitudes: no land-sea contrast or high

mountain ranges in the meridional direction (less wave sources), and a stronger and more stable

polar vortex that does not allow waves to propagate so deep into high latitudes, as opposed to the

NH. The behavior of the extratropical wave forcing in SH polar latitudes (Fig. 8) is similar to the

525   NH (Fig. 6) but weaker. In subsection 4.2 (NH polar latitudes) it was shown that, after subtracting

the extratropical wave signal, the TIL enhancement from SSWs (major or minor) and final warmings could be seen clearly. In the 2007-2013 period, no SSW occurred in the SH, so we only aim to see what is the effect of final warmings.

Figure 9a shows the daily evolution of the tropopause-based N^2 profile at 80°S. There is a clear TIL during summer months, with N^2 values of $\sim 7 \times 10^{-4} s^{-2}$ (brown) right above the tropopause. In winter, the TIL is harder to discern, but a weak maximum of $\sim 4.5 \times 10^{-4} s^{-2}$ (white, light yellow) is present above the winter tropopause. The TIL near the South Pole in winter is known to be very weak or absent (Tomikawa et al., 2009; Pilch Kedzierski et al., 2015). Compared to the NH, the SH polar vortex is stronger, less disturbed during winter, and has a longer lifetime: it breaks later in spring, almost into the summer.

Note that in Fig. 9 the tropopause is higher during winter (unlike in Figs. 5 and 7). This seasonal cycle in the high-latitude SH tropopause agrees with previous climatologies from GPS-RO (Son et al., 2011), and is attributed to the very cold and stable polar vortex (Zängl and Hoinka, 2001) and the seasonal cycle in the strength of the Brewer-Dobson circulation (Yulaeva et al., 1994). Also, there is some indeterminacy in the exact height of the thermal tropopause, since the background temperature lapse-rate in SH high-latitudes is close to the WMO lapse-rate tropopause criterion (WMO, 1957) of 2K/km for several kilometers in the upper troposphere during winter. We discuss the downward-propagating signal of the SH polar vortex breakup next.

Fig. 9b shows the N^2 profile evolution without the daily extratropical wave signal, displaying the tropopause-based N^2 structures caused by other processes. In summer, the TIL is significantly weaker but clearly present in Fig. 9b. In winter, the TIL cannot be detected without the extratropical wave signal, and the vertical N^2 structures are smoother and enable a clearer view of the downward-propagating N^2 signal from the SH vortex breakup in late spring. Once the signal reaches the tropopause region, there is an abrupt increase in N^2 right above the tropopause, from values of $\sim 4 \times 10^{-4} s^{-2}$ (blue) to $\sim 5.5 \times 10^{-4} s^{-2}$ (yellow-orange), in line with the findings of Wargan and Coy (2016) and our previous subsection 4.2 and Fig. 7b. Even a slight and short-lived relative minimum in tropopause height can be observed with the arrival of the vortex breakup signal. Note that in Fig. 9b, no TIL is discernible until the downward-propagating N^2 signal from the SH polar vortex breakup arrives. For example, the contrast between the summers of 2011/12 and 2012/13: in the first summer, the signal reaches the tropopause region right at the beginning of 2012, and the TIL is observed since; whereas in the next summer the polar vortex breaks up early, and the strong TIL is observed more than a month before the beginning of 2013.

Later in the summer, the TIL generally reaches N^2 values of $\sim 6 \times 10^{-4} s^{-2}$ every year in Fig. 9b. As in the previous subsection 4.2, we also suggest that the remaining TIL in Fig. 9b in summer is enhanced by water vapor radiative effects which would need further study.

5   Concluding Remarks

Our study used a simplified method to extract the total extratropical (planetary to synoptic-scale) wave signal from gridded COSMIC GPS-RO profiles. By tropopause-based zonal averaging of these signals at certain latitude bands, we were able to quantify how much of the extratropical TIL at
565   mid- and polar latitudes is explained by the instantaneous modulation of the tropopause region by the planetary and synoptic-scale waves. By subtracting the extratropical wave signal, we show how much of the TIL is left due to other processes.

We found that extratropical wave modulation explains almost all of the observed TIL strength at mid-latitudes in both hemispheres (Figs. 5 and A2). Therefore we conclude that wave-mean flow in-
570   teractions, inertia-gravity waves or the residual circulation are of minor importance as TIL enhancing mechanisms there.

At polar regions, extratropical wave modulation is dominant as well in explaining the TIL strength, but there is also a clear signal from SSWs, major and minor, in the Northern Hemisphere, and final warmings in both hemispheres (Figs. 7 and 9). The similarity in the time evolution of all signals
575   from the disturbed polar vortexes in both hemispheres suggests that they are forced by the same mechanism: $\overline{w*}$ convergence from accelerated residual circulation as in the major SSW study by Wargan and Coy (2016).

Also, part of the polar summer TIL strength is not explained by extratropical wave modulation nor by residual circulation. We suggest that the only other mechanism restricted to polar summer that
580   could enhance the TIL is water vapor radiative cooling of the tropopause (Randel and Wu, 2010; Miyazaki et al., 2010b), which requires additional study to be confirmed.

Two questions arise from our results: 1) what are the separate roles of the different planetary and synoptic-scale wave types within the total extratropical wave modulation of the TIL, and 2) which is the mechanism for wave amplification near the tropopause as seen in Fig. 3.
585   Our study, working only with COSMIC GPS-RO observations, has identified and quantified an important mechanism for extratropical TIL enhancement: extratropical wave modulation, which is dominant in the extratropics and especially at mid-latitudes. We suggest that the remaining TIL in polar regions can be explained by accelerated residual circulation from polar vortex disturbances (given the similarities of our results with Wargan and Coy (2016)) and water vapor radiative effects
590   in polar summer, although these would need to be confirmed by additional studies.

Appendix A: Wave modulation of the TIL in SH Mid-latitudes

Figure A1 is the Southern Hemisphere equivalent of Fig. 4 (which was for 40°N). The signatures of the different extratropical waves in Fig. A1 lead to the same conclusions for the SH mid-latitudes: all defined waves show a net cooling effect maximizing at the tropopause, a slight warming above
595   it, and a net N^2 increase directly above the tropopause (Fig. A1 a-d). The strongest wave signal

belongs to eastward-propagating waves with periods of 4 to 25 days (red lines), which is even more dominant in Fig. A1 than in Fig. 4 due to the stronger westerlies found in the SH. Quasi-stationary waves (periods of 30-96 days, black and dashed magenta lines) and the s=0 wave type (grey line) play a minor role in enhancing the TIL in both hemispheres.

600   The total extratropical wave signal (Fig. A1 e-f) at 40°S is a ∼3.6K colder tropopause in the seasonal zonal-mean, tropopause-based profile, and a TIL enhancement of ∼$1.7 \times 10^{-4} s^{-2}$ in winter (red line). In summer (black line) the modulation is weaker: tropopause cooling of ∼3.0K and ∼$1.4 \times 10^{-4} s^{-2}$ of TIL enhancement. The total extratropical wave signature in SH mid-latitudes has the same winter-summer seasonality as the NH, and a slightly higher magnitude throughout the year.

605   Figure A2 compares the daily evolution of the zonal-mean, tropopause-based vertical N^2 profile at 40°S, with (Fig. A2a) and without the extratropical wave signal (Fig. A2b). Fig. A2 is the SH equivalent of Fig. 5, and also leads to the same conclusions: there is a distinct TIL in Fig. A2a throughout the year (∼$6 \times 10^{-4} s^{-2}$, orange-red in winter; ∼$5 \times 10^{-4} s^{-2}$ yellow in summer), which is almost completely gone once the daily extratropical wave signal is subtracted. The weak hints of a

610   TIL seen in Fig. 5b are even weaker in Fig. A2b, suggesting that other TIL enhancing processes play an even humbler role in the SH. We conclude from Fig. A2 that the TIL modulation by planetary and synoptic-scale waves explains most of the TIL strength in the tropopause-based N^2 structure at mid-latitudes also in the SH.

The findings of subsection 4.1 (NH mid-latitudes, Figs. 4 and 5) also apply to the SH (Figs. A1

615   and A2) in a nearly-coincident way.

Acknowledgements. This study was completed within the Helmholtz-University Young Investigators Group NATHAN project, funded by the Helmholtz Association through the president's Initiative and Networking Fund and the GEOMAR Helmholtz-Centre for Ocean Research in Kiel. We thank the ECMWF data server for the freely available ERA-Interim data; and UCAR for the COSMIC, satellite missions' temperature profiles.

620   The assistance accessing different datasets and discussions with Sandro Lubis, Wuke Wang and Sebastian Wahl are also appreciated.

References

Andrews, D. G., Holton, J. R., and Leovy, C. B.: Middle atmosphere dynamics, International Geophysics Series, Vol. 40, Academic Press, 1987.

Anthes, R. A., Bernhardt, P. A., Chen, Y., Cucurull, L., Dymond, K. F., Ector, D., Healy, S. B., Ho, S.-P., Hunt, D. C., Kuo, Y.-H., Liu, H., Manning, K., McCormick, C., Meehan, T. K., Randel, W. J., Rocken, C., Schreiner, W. S., Sokolovskiy, S. V., Syndergaard, S., Thompson, D. C., Trenberth, K. E., Wee, T.-K., Yen, N. L., and Zeng, Z.: The COSMIC/FORMOSAT-3 Mission: Early Results, Bulletin of the American Meteorological Society, 89, 313, doi:10.1175/BAMS-89-3-313, 2008.

Birner, T.: Fine-scale structure of the extratropical tropopause region, Journal of Geophysical Research (Atmospheres), 111, D04104, doi:10.1029/2005JD006301, 2006.

Birner, T.: Residual Circulation and Tropopause Structure, Journal of Atmospheric Sciences, 67, 2582–2600, doi:10.1175/2010JAS3287.1, 2010.

Birner, T., Dörnbrack, A., and Schumann, U.: How sharp is the tropopause at midlatitudes?, Geophysical Research Letters, 29, 1700, doi:10.1029/2002GL015142, 2002.

Dee, D. P., Uppala, S. M., Simmons, A. J., Berrisford, P., Poli, P., Kobayashi, S., Andrae, U., Balmaseda, M. A., Balsamo, G., Bauer, P., Bechtold, P., Beljaars, A. C. M., van de Berg, L., Bidlot, J., Bormann, N., Delsol, C., Dragani, R., Fuentes, M., Geer, A. J., Haimberger, L., Healy, S. B., Hersbach, H., Hólm, E. V., Isaksen, L., Kållberg, P., Köhler, M., Matricardi, M., McNally, A. P., Monge-Sanz, B. M., Morcrette, J.-J., Park, B.-K., Peubey, C., de Rosnay, P., Tavolato, C., Thépaut, J.-N., and Vitart, F.: The ERA-Interim reanalysis: configuration and performance of the data assimilation system, Quarterly Journal of the Royal Meteorological Society, 137, 553–597, doi:10.1002/qj.828, 2011.

Erler, A. R. and Wirth, V.: The Static Stability of the Tropopause Region in Adiabatic Baroclinic Life Cycle Experiments, Journal of Atmospheric Sciences, 68, 1178–1193, doi:10.1175/2010JAS3694.1, 2011.

Gettelman, A., Hoor, P., Pan, L. L., Randel, W. J., Hegglin, M. I., and Birner, T.: The Extratropical Upper Troposphere and Lower Stratosphere, Reviews of Geophysics, 49, RG3003, doi:10.1029/2011RG000355, 2011.

Grise, K. M., Thompson, D. W. J., and Birner, T.: A Global Survey of Static Stability in the Stratosphere and Upper Troposphere, Journal of Climate, 23, 2275–2292, doi:10.1175/2009JCLI3369.1, 2010.

Hegglin, M. I., Boone, C. D., Manney, G. L., and Walker, K. A.: A global view of the extratropical tropopause transition layer from Atmospheric Chemistry Experiment Fourier Transform Spectrometer O_3, H_2O, and CO, Journal of Geophysical Research (Atmospheres), 114, D00B11, doi:10.1029/2008JD009984, 2009.

Kunkel, D., Hoor, P., and Wirth, V.: Can inertia-gravity waves persistently alter the tropopause inversion layer?, Geophysical Research Letters, 41, 7822–7829, doi:10.1002/2014GL061970, 2014.

Kunz, A., Konopka, P., Müller, R., Pan, L. L., Schiller, C., and Rohrer, F.: High static stability in the mixing layer above the extratropical tropopause, Journal of Geophysical Research (Atmospheres), 114, D16305, doi:10.1029/2009JD011840, 2009.

Kursinski, E. R., Hajj, G. A., Schofield, J. T., Linfield, R. P., and Hardy, K. R.: Observing Earth's atmosphere with radio occultation measurements using the Global Positioning System, Journal of Geophysical Research: Atmospheres, 102, 23 429–23 465, doi:10.1029/97JD01569, 1997.

Miyazaki, K., Watanabe, S., Kawatani, Y., Sato, K., Tomikawa, Y., and Takahashi, M.: Transport and Mixing in the Extratropical Tropopause Region in a High-Vertical-Resolution GCM. Part II: Relative Importance of Large-Scale and Small-Scale Dynamics, Journal of Atmospheric Sciences, 67, 1315–1336, doi:10.1175/2009JAS3334.1, 2010a.

665 Miyazaki, K., Watanabe, S., Kawatani, Y., Tomikawa, Y., Takahashi, M., and Sato, K.: Transport and Mixing in the Extratropical Tropopause Region in a High-Vertical-Resolution GCM. Part I: Potential Vorticity and Heat Budget Analysis, Journal of Atmospheric Sciences, 67, 1293–1314, doi:10.1175/2009JAS3221.1, 2010b.

Pilch Kedzierski, R., Matthes, K., and Bumke, K.: Synoptic-scale behavior of the extratropical tropopause inversion layer, Geophysical Research Letters, 42, 10,018–10,026, doi:10.1002/2015GL066409, 2015GL066409,

670 2015.

Pilch Kedzierski, R., Matthes, K., and Bumke, K.: The Tropical Tropopause Inversion Layer, Atmospheric Chemistry and Physics Discussions, pp. 1–26, doi:10.5194/acp-2016-178, 2016.

Randel, W. J. and Wu, F.: Kelvin wave variability near the equatorial tropopause observed in GPS radio occultation measurements, Journal of Geophysical Research (Atmospheres), 110, D03102,

675 doi:10.1029/2004JD005006, 2005.

Randel, W. J. and Wu, F.: The Polar Summer Tropopause Inversion Layer, Journal of Atmospheric Sciences, 67, 2572–2581, doi:10.1175/2010JAS3430.1, 2010.

Randel, W. J., Wu, F., and Forster, P.: The Extratropical Tropopause Inversion Layer: Global Observations with GPS Data, and a Radiative Forcing Mechanism, Journal of Atmospheric Sciences, 64, 4489,

680 doi:10.1175/2007JAS2412.1, 2007.

Schmidt, T., Cammas, J.-P., Smit, H. G. J., Heise, S., Wickert, J., and Haser, A.: Observational characteristics of the tropopause inversion layer derived from CHAMP/GRACE radio occultations and MOZAIC aircraft data, Journal of Geophysical Research (Atmospheres), 115, D24304, doi:10.1029/2010JD014284, 2010.

Schreck, C.: Extract equatorial waves by filtering in the Wheeler-Kiladis wavenumber-frequency domain., https:

685 //www.ncl.ucar.edu/Document/Functions/User_contributed/kf_filter.shtml, 2009.

Sjoberg, J. P. and Birner, T.: Stratospheric Wave-Mean Flow Feedbacks and Sudden Stratospheric Warmings in a Simple Model Forced by Upward Wave Activity Flux, Journal of Atmospheric Sciences, 71, 4055–4071, doi:10.1175/JAS-D-14-0113.1, 2014.

Son, S.-W. and Polvani, L. M.: Dynamical formation of an extra-tropical tropopause inversion

690 layer in a relatively simple general circulation model, Geophysical Research Letters, 34, L17806, doi:10.1029/2007GL030564, 2007.

Son, S.-W., Tandon, N. F., and Polvani, L. M.: The fine-scale structure of the global tropopause derived from COSMIC GPS radio occultation measurements, Journal of Geophysical Research (Atmospheres), 116, D20113, doi:10.1029/2011JD016030, 2011.

695 Tomikawa, Y., Nishimura, Y., and Yamanouchi, T.: Characteristics of Tropopause and Tropopause Inversion Layer in the Polar Region, SOLA, 5, 141–144, doi:10.2151/sola.2009-036, 2009.

Wargan, K. and Coy, L.: Strengthening of the Tropopause Inversion Layer during the 2009 Sudden Stratospheric Warming: A MERRA-2 Study, Journal of Atmospheric Sciences, 73, 1871–1887, doi:10.1175/JAS-D-15-0333.1, 2016.

700 Wheeler, M. and Kiladis, G. N.: Convectively Coupled Equatorial Waves: Analysis of Clouds and Temperature in the Wavenumber-Frequency Domain., Journal of Atmospheric Sciences, 56, 374–399, doi:10.1175/1520-0469(1999)056<0374:CCEWAO>2.0.CO;2, 1999.

Wirth, V.: Static Stability in the Extratropical Tropopause Region., Journal of Atmospheric Sciences, 60, 1395–1409, doi:10.1175/1520-0469(2003)060<1395:SSITET>2.0.CO;2, 2003.

705 Wirth, V.: A dynamical mechanism for tropopause sharpening, Meteorologische Zeitschrift, 13, 477–484, doi:10.1127/0941-2948/2004/0013-0477, 2004.

Wirth, V. and Szabo, T.: Sharpness of the extratropical tropopause in baroclinic life cycle experiments, Geophysical Research Letters, 34, 2809, doi:10.1029/2006GL028369, 2007.

WMO: Meteorology-A three-dimensional science, WMO Bull., 6, 134–138, 1957.

710 WMO: Guide to Meteorological Instruments and Methods of Observation, 6th ed. WMO No. 8, 1996.

Yulaeva, E., Holton, J. R., and Wallace, J. M.: On the Cause of the Annual Cycle in Tropical Lower-Stratospheric Temperatures., Journal of Atmospheric Sciences, 51, 169–174, doi:10.1175/1520-0469(1994)051<0169:OTCOTA>2.0.CO;2, 1994.

Zängl, G. and Hoinka, K. P.: The Tropopause in the Polar Regions., Journal of Climate, 14, 3117–3139,

715 doi:10.1175/1520-0442(2001)014<3117:TTITPR>2.0.CO;2, 2001.

Zhang, Y., Zhang, S., Huang, C., Huang, K., Gong, Y., and Gan, Q.: The interaction between the tropopause inversion layer and the inertial gravity wave activities revealed by radiosonde observations at a midlatitude station, Journal of Geophysical Research: Atmospheres, 120, 8099–8111, doi:10.1002/2015JD023115, 2015.
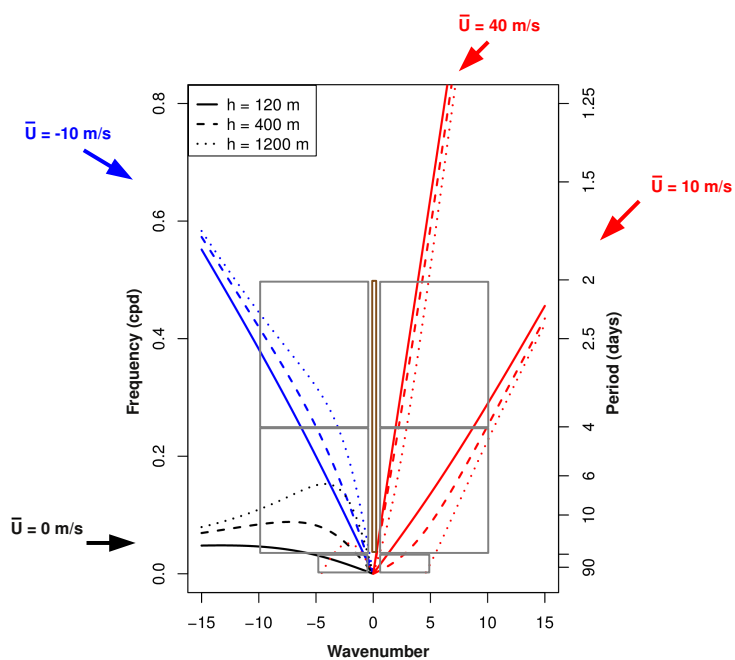
Figure 1. Dispersion curves for forced Planetary Waves at 50°N under different mean zonal wind regimes (line colors, winds specified outside the diagram), and differentiating equivalent depths (line type, top-left box). Filter bounds in the wavenumber-frequency domain are shown as grey boxes (brown for wavenumber zero).
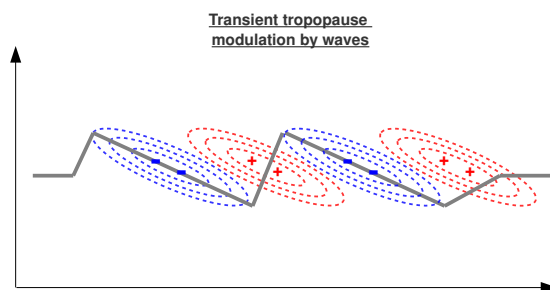
Figure 2. Schematic of transient tropopause modulation by an idealized wave with westward vertical tilt, as a snapshot of the wave's temperature anomalies (dashed contours: positive red, negative blue) and the undulating tropopause (thick and solid grey line).
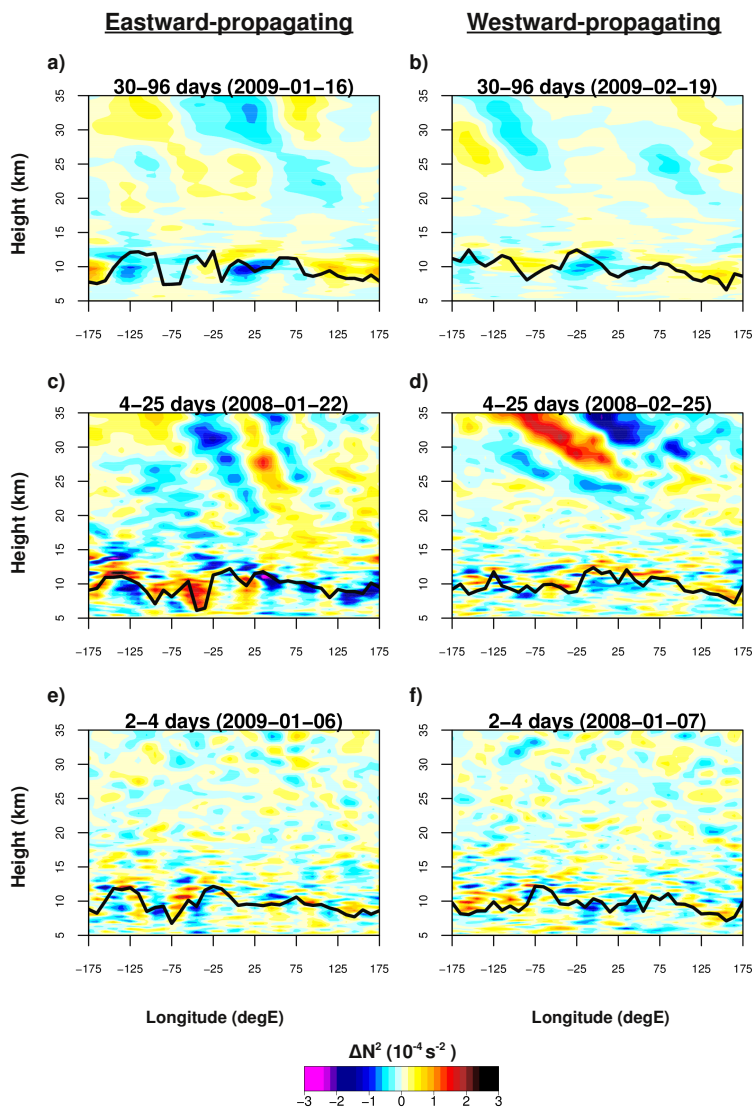
Figure 3. Longitude-height snapshots of the N^2 anomalies of the different wave types at certain dates, for the 50°N latitude band. Wave types correspond to the wavenumber-frequency domains defined in Fig. 1, except for wavenumber zero. Left column are eastward-propagating waves, right column are westward-propagating waves, and their periods are specified along with the date. The black line denotes the thermal tropopause.
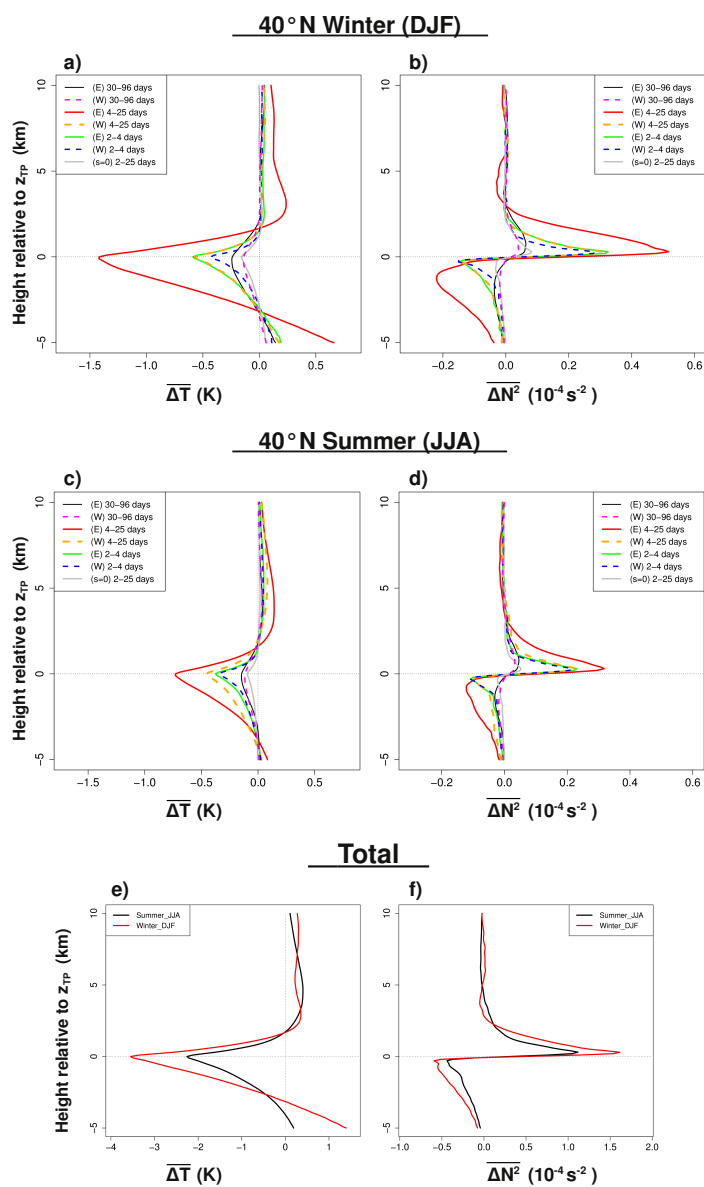
Figure 4. Average signature of the different wave types at 40°N, as the mean anomaly in the zonal-mean vertical profiles of temperature ($\overline{\Delta T}$, left column) and static stability ($\overline{\Delta N^2}$, right column). Top row (a and b) for winter (DJF), middle row (c and d) for summer (JJA). Bottom row (e and f) compares the total seasonal wave signatures.
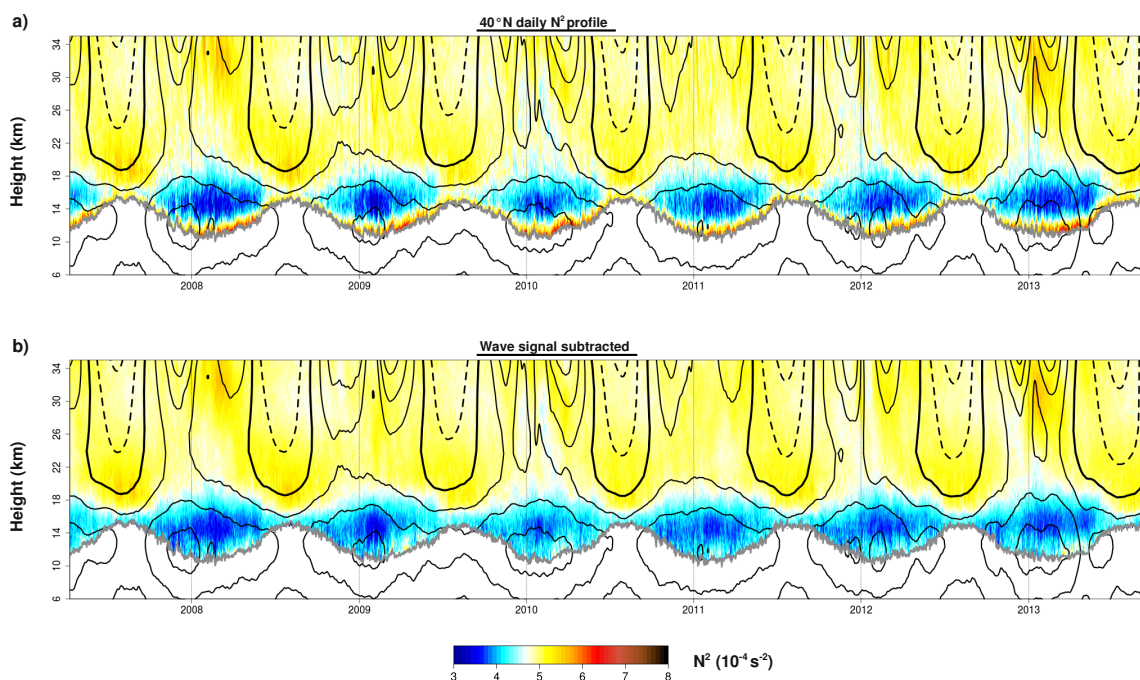
Figure 5. a) Daily evolution of the tropopause-based, 40°N zonal mean N^2 vertical profile between 2007-2013 (colors) from COSMIC GPS-RO profiles. The grey line denotes the tropopause height (TP_z). Thin black contours denote positive (westerly) mean zonal wind, with a thicker contour for the zero line, dashed contours for negative (easterly) winds, and a 10m/s separation. To improve visibility, the winds are displayed with a running mean of +-15 days. No running mean is applied to the N^2 vertical profile or TP_z in order to allow the subtraction of the extratropical wave signal. b) Same as in Fig. 5a, but the daily wave signal has been subtracted from the N^2 vertical profile.
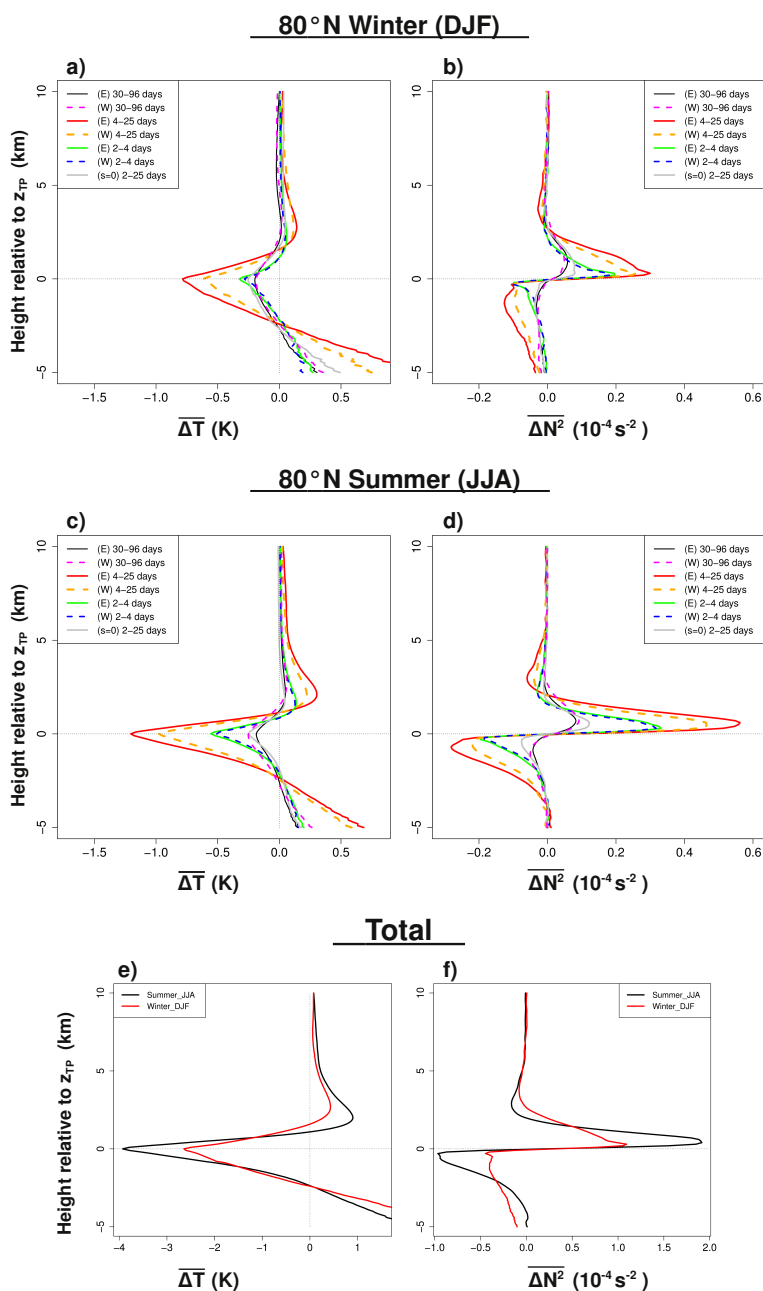
Figure 6. As in Fig. 4, but for 80°N.
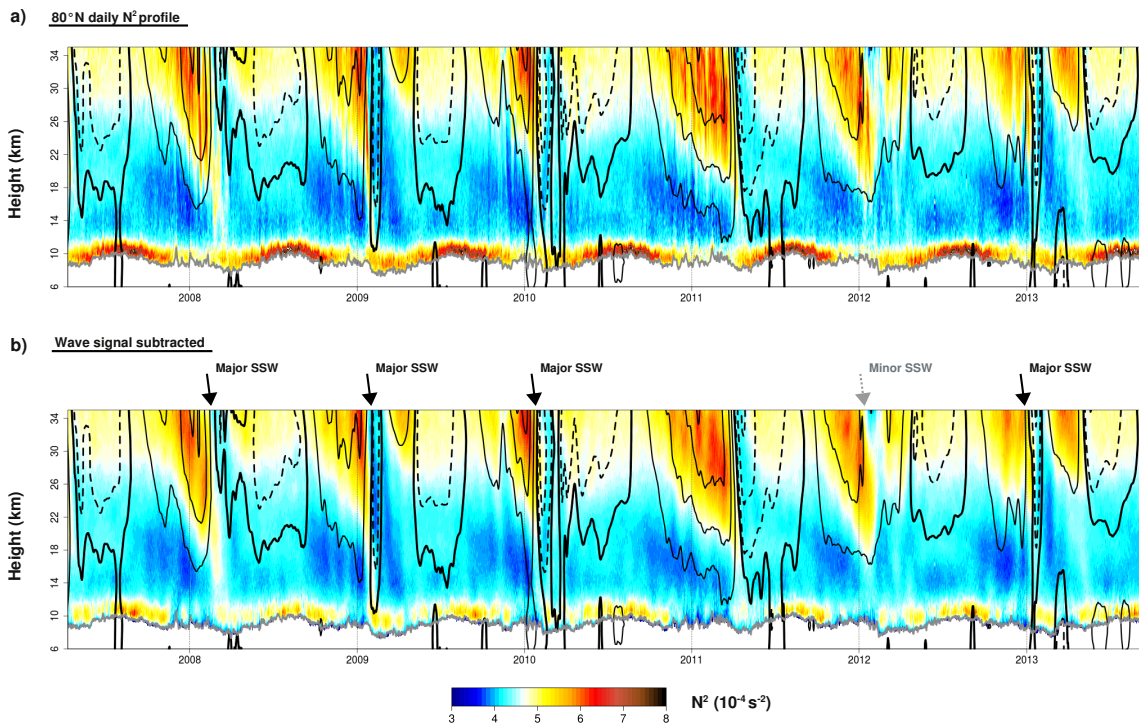
Figure 7. As in Fig. 5, but for 80°N. Major and minor SSWs are marked above Fig. 7b. First easterly wind contour (dashed line) at -3m/s for better visibility. The rest of wind contours are 10m/s intervals as in Fig. 5.
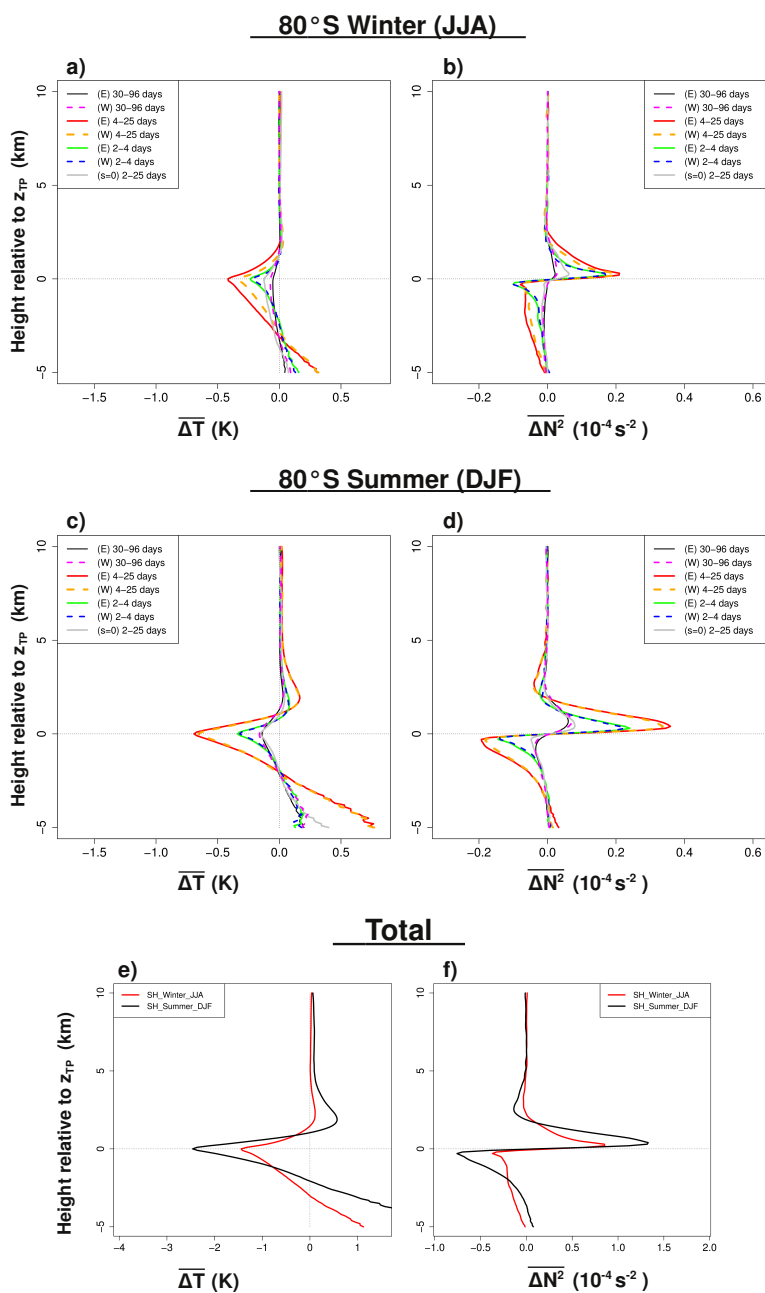
Figure 8. As in Figs. 4 and 6, but for 80°S.
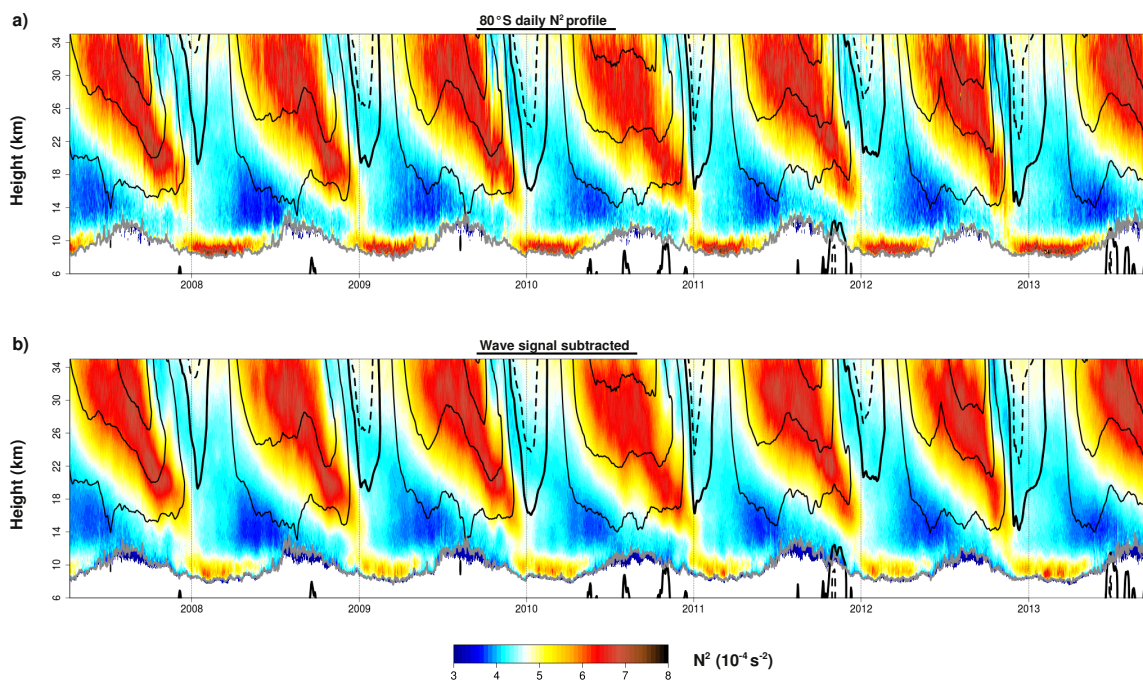
Figure 9. As in Fig. 5 and 7, but for 80°S. First easterly wind contour (dashed line) at -3m/s for better visibility.
The rest of wind contours are 10m/s intervals as in Fig. 5.
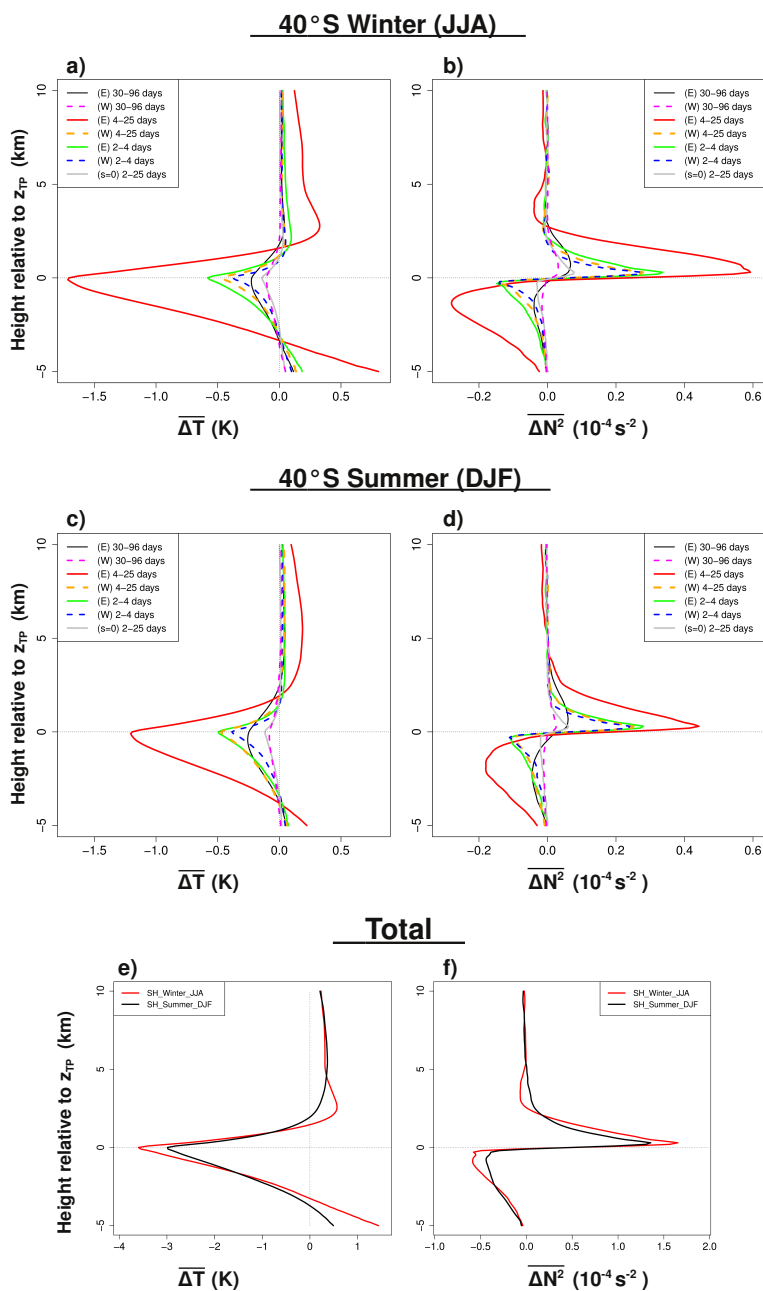
Figure A1. As in Figs. 4, 6 and 8, but for 40°S.
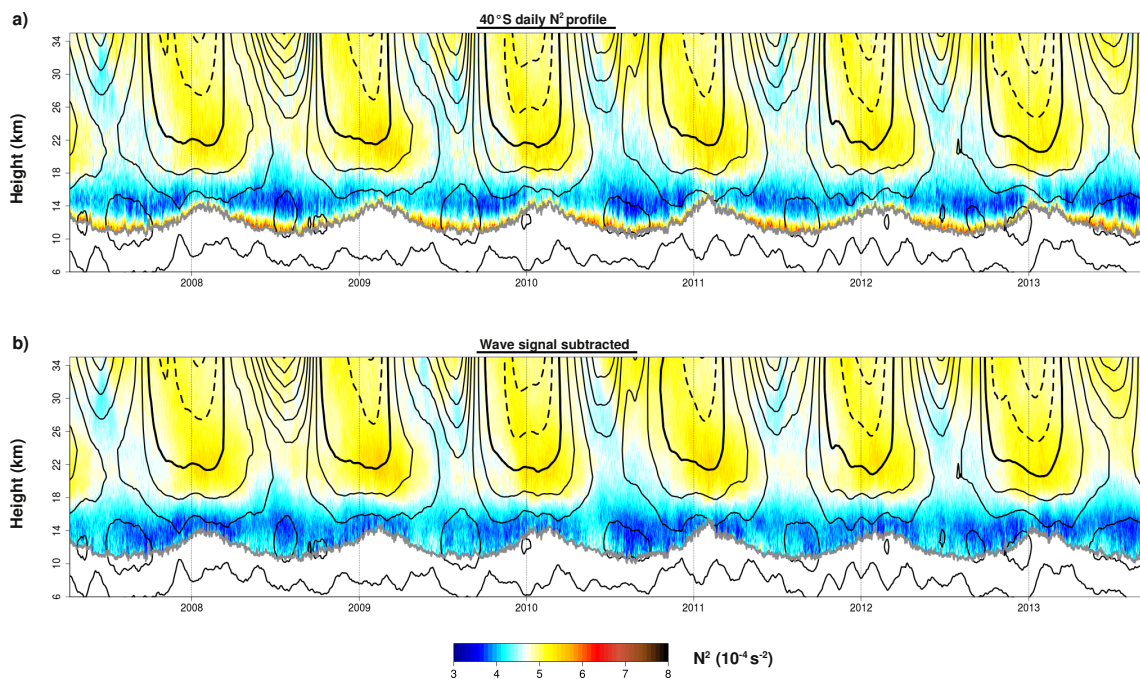
Figure A2. As in Fig. 5, but for 40°S.